Nanoscale

PAPER

View Article Online
View Journal | View Issue

Cite this: *Nanoscale*, 2016, **8**, 10632

A microwave synthesized Cu_xS and graphene oxide nanoribbon composite as a highly efficient counter electrode for quantum dot sensitized solar cells†

Dibyendu Ghosh, Ganga Halder, Atharva Sahasrabudhe and Sayan Bhattacharyya*

Received 9th February 2016,
Accepted 20th April 2016

DOI: 10.1039/c6nr01161f

www.rsc.org/nanoscale

To boost the photoconversion efficiency (PCE) of ever promising quantum dot sensitized solar cells (QDSSCs), and to improve the design of photoanodes, the ability of the counter electrode (CE) to effectively reduce the oxidized electrolyte needs special attention. A composite of a 15 wt% graphene oxide nanoribbon (GOR), obtained by unzipping multi-walled carbon nanotubes (MWCNTs), and Cu_xS intersecting hexagonal nanoplates, synthesized by a low cost, facile and scalable microwave synthesis route, is reported as a fascinating CE for QDSSCs. The best performing $Cu_{1.18}S$–GOR CE could notably achieve a record PCE of ~3.55% for CdS sensitized QDSSCs, ~5.42% for *in situ* deposited CdS/CdSe co-sensitized QDSSCs and ~6.81% for CdTe/CdS/CdS dual sensitized QDSSCs, apart from increasing the PCE of previously reported QDSSCs. A systematic investigation of the CE design revealed the high electrocatalytic activity of GOR due to the presence of organic functional groups, graphitic edge sites and a quasi-one-dimensional (quasi-1D) structure, which increases the interfacial charge transfer kinetics from the CE to the polysulfide electrolyte. The highly stable $Cu_{1.18}S$–GOR CE has the added advantage of a favourable energy band alignment with the redox potential of the polysulfide electrolyte, which reduces the loss of charge carriers and thus can increase the PCE of QDSSCs.

1. Introduction

The low cost third generation solar cells fabricated using semiconductor quantum dots (QDs) as light harvesters are extremely appealing because of the solution processability of QDs and their tunable band gap, high absorption coefficient and possibilities of multiple exciton generation.[1,2] Although overshadowed by the rapidly increasing efficiencies of organometal halide perovskite solar cells,[3] quantum dot sensitized solar cells (QDSSCs) have started to demonstrate promising PCE,[4–9] whereas the current efficiency scenario for QDSSC has just reached above 9% for the liquid junction QDSSC,[10] and 10.7% for the solid state device.[11] To improve the overall performance, all three basic components of QDSSCs, *viz.* the photoanode,[12–15] the electrolyte,[16,17] and the CE,[18–22] need to be optimized. The role of a CE is to collect electrons from the external circuit and catalytically reduce the redox electrolyte, the latter being oxidized after hole scavenging from the sensitizer. In the popularly used polysulfide electrolyte, an ideal CE should be stable without any sulfur poisoning, possess high electrocatalytic activity, pose lower charge-transfer resistance at the CE–electrolyte interface and be cost-effective.

Pt CEs are prone to surface adsorb sulphur atoms from the polysulfide electrolytes, which decreases their conductivity and electrocatalytic reducing property, thereby affecting the PCE of QDSSCs.[23] A large variety of replacement materials, such as Cu_xS,[24–27] Co–S,[28,29] NiS,[30] PbS,[31,32] Bi_2S_3,[33] Cu_2ZnSnS_4,[34] and carbon–Cu_xS composites,[18,23] have been investigated for designing next-generation CEs. Cu_xS and its composite with different carbon allotropes show better performance and stability. Recently a CuS/$Cu_{1.8}S$ CE was reported for a CdSe-sensitized solar cell to attain 6.28% PCE,[35] and $FeSe_2$, $Cu_{1.8}S$, and CuSe films were reported as efficient CEs for both dye-sensitized solar cells (DSSCs) and QDSSCs.[36] As composites with carbon, the highly catalytic reduced graphene oxide (RGO)–Cu_2S CE with the CdS/CdSe co-sensitizer had a PCE of 4.4%;[18] however, with a similar photoanode, CuS and $Cu_{1.8}S$ nanosheet arrays as CEs achieved a PCE of 6.53%.[37] Other than a chalcogenide based CE, composites of carbon dots and Au nanoraspberries achieved ~5.4% PCE with a ZnO nanowire/CdS/CdSe photoanode.[38]

In fact, the 2D carbon nanostructure GOR with superior electrical, optical, thermal, and mechanical properties is useful as a hole extracting layer as well as electron blocking layer in solar cells.[39,40] GORs with high aspect ratios and quasi-1D confinement of charge carriers are narrow elongated

Department of Chemical Sciences, Indian Institute of Science Education and Research (IISER) Kolkata, Mohanpur, 741246, India. E-mail: sayanb@iiserkol.ac.in

†Electronic supplementary information (ESI) available. See DOI: 10.1039/c6nr01161f

strips of graphene oxide (GO) with large catalytic edges and prepared by unzipping CNTs.[40,41] GOR has larger surface area for interaction with the electrolyte and chalcogenide nanostructures than the parent CNTs, GO or RGO, conveniently prepared by greener routes.[42] Even if GOR shows unique solution processability, there has been no report offering an optimization of the metal chalcogenide and the GOR composite that can offer high electrocatalytic performance as a CE in QDSSCs. The catalytic performance of the CE in QDSSCs depends on the available active sites and how fast the electrons flow back into the electrolyte from the external circuit, creating electron pathways to complete the circuit. So the carrier mobility of a CE should be good enough to reduce the charge transfer resistance (R_{CT}). R_{CT} will add up to the overall series resistance (R_s), which determines the most important parameter of QDSSC, the fill factor (FF). So the catalytically efficient CE will reduce R_s and improve FF, resulting in a higher PCE. GOR offers one of the greatest intrinsic carrier mobilities at room temperature, with a perfect atomic lattice, a promising mechanical strength, and chemical and thermal stability with additional functionalization of –OH and –COOH groups.

Previously the Cu_xS CE was prepared *via* exposing a brass foil to the polysulfide electrolyte,[43,44] electrochemical deposition,[45] electrospinning,[46] solvothermal,[47] successive ion layer adsorption and reaction (SILAR) *etc*.[48] Unlike the detailed synthesis strategies involving surfactants, organic solvents and an inert atmosphere required for controlling the domain sizes and topologies,[49] in this report a low cost microwave irradiation technique was used for the scalable production of Cu_xS nanostructures with a tunable chemical composition, whereas GOR was synthesized by oxidative unzipping of MWCNTs. The superiority of GOR as a composite material over GO and CNTs is discussed based on electrochemical experiments. The CE made by doctor blading a paste of Cu_xS–GOR composite on FTO glass shows enhanced catalytic activity, which is stable over several cycles and could improve the PCE of reported QDSSCs.

2. Results and discussion

In this section, after individual characterizations of the Cu_xS and carbon nanostructures, the design of the optimized CE will be discussed in the following steps: (i) to optimize the Cu:S stoichiometry for the best photovoltaic and catalytic activity of Cu_xS, (ii) to investigate the reason why GOR is a superior composite material over CNTs and GO, and (iii) to optimize the weight% of GOR with respect to Cu_xS. Finally the optimized Cu_xS–GOR CE will be demonstrated to increase the PCE of reported photoanodes.

2.1 Characterization of the individual components of CE

2.1.1 Cu_xS nanostructures. Fig. 1a shows the X-ray diffraction (XRD) patterns of seven different compositions of Cu_xS nanostructures. The XRD reflections match with the hexagonal crystal structure of covellite Cu_xS (JCPDS no. 06-0464). The

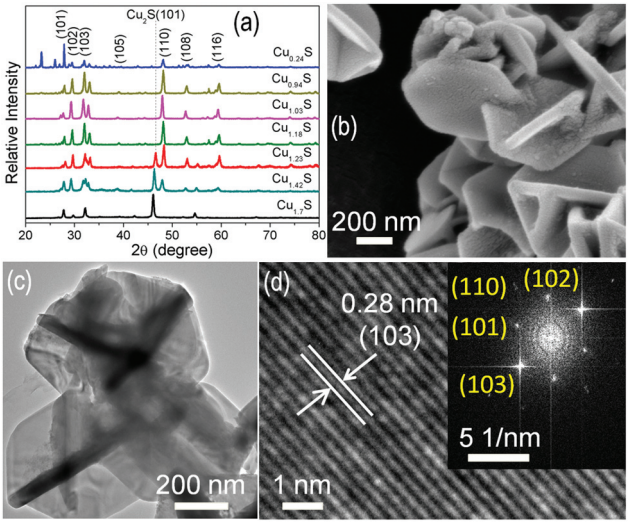

Fig. 1 (a) XRD spectra of Cu_xS nanostructures. (b) FESEM and (c) TEM images of $Cu_{1.18}S$ nanostructures. (d) High resolution TEM image showing the interplanar spacing of $Cu_{1.18}S$ and the inset shows the SAED pattern.

reflection at $2\theta = 46.5°$ for the (101) plane is observed for Cu/S ratio >1.18 due to the formation of the chalcocite Cu_2S phase (JCPDS no. 01-0831462). In $Cu_{1.42}S$ the (101) reflection increases at the cost of the (110) reflection at $2\theta = 47.9°$, which is more prominent in $Cu_{1.7}S$. The Cu:S stoichiometry was confirmed from the energy dispersive analysis of X-ray (EDAX) spectra recorded over 6 areas on each Cu_xS sample (ESI, Fig. S1†). Elemental mapping confirms the uniform composition of Cu:S over the entire nanostructure (Fig. S1h†). Fig. 1b shows a field emission scanning electron microscope (FESEM) 3-dimensional image of the representative $Cu_{1.18}S$ nanostructure. The Cu_xS nanostructures are composed of intersecting hexagonal nanoplates, the thickness of which increases from ~50 nm for $x = 0.24$ to ~80 nm for $x = 1.03$ and thereafter remains constant at 55–65 nm for $x = 1.18$–1.7 (Fig. S2†). Two of the major changes with increasing Cu/S ratio are the decrease in lateral dimension of the plates, say from >2 μm for $Cu_{0.24}S$ to ~200 nm for $Cu_{1.7}S$, and the gradual increase in roughness of the smaller plates at low S content. At a mean Cu/S ratio of $x = 1.18$, the diameter of the moderately rough surfaced plates is ~600 nm and the thickness of the plates remains at ~57 nm. Fig. 1c shows the transmission electron microscopy (TEM) image of $Cu_{1.18}S$ and the interplanar spacing corresponding to $d_{102} = 0.28$ nm is observed in Fig. 1d. The corresponding selected area electron diffraction (SAED) pattern (inset of Fig. 1d) shows the high crystallinity of $Cu_{1.18}S$ nanoplates.

2.1.2 Carbon nanostructures: CNT, GO and GOR. The commercial MWCNT (Fig. 2a) was unzipped by oxidative cleavage to produce GOR (Fig. 2b) whereas GO (Fig. 2c) was synthesized by the modified Hummers method. The TEM image of GOR (Fig. 2d) shows a multifaceted disordered structure with a distinct CNT wall opening giving rise to the ribbon-like morphology. As observed in the XRD patterns in Fig. 2e, the

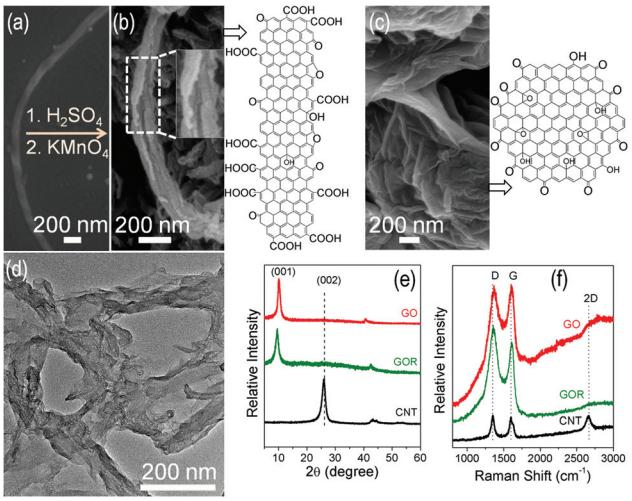

Fig. 2 (a) FESEM image of a single CNT. FESEM images and schematics of (b) GOR synthesized by unzipping CNT (enlarged view shown in the inset) and (c) GO. (d) TEM image of GOR. (e) XRD and (f) Raman spectra of CNT, GOR and GO.

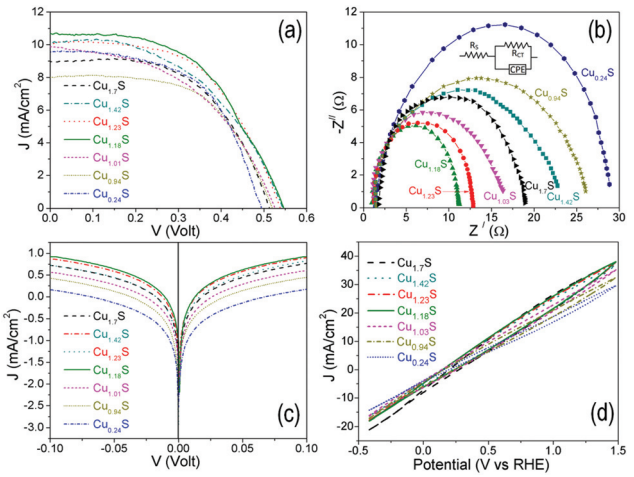

Fig. 3 (a) J–V characteristics of a representative CdS sensitized photoanode with different Cu_xS CEs. (b) Nyquist plot and (c) Tafel polarization characteristics measured with a symmetric dummy cell. The inset of (b) shows the equivalent circuit where CPE stands for the constant phase element. (d) CV plots measured with a conventional three electrode cell for seven different Cu_xS nanostructures as the working electrode.

graphitic (002) reflection of the CNTs at $2\theta \sim 26.08°$ (JCPDS no. 75-1621) is absent in GO and GOR and a new peak at $2\theta \sim 9.56°$ corresponding to the (001) plane (JCPDS no. 89-8487) appears. The appearance of the (001) reflection and the absence of the (002) peak indicate the successful unzipping and exfoliation of the graphitic sheets into graphene oxide layers.[40,50] Room temperature Raman spectra (Fig. 2f) show the disorder induced D-band at 1355 cm^{-1} and the G-band corresponding to the phonon stretching mode of the sp^2 carbon atoms at 1599 cm^{-1}. The intensity ratio of D and G bands increases from the CNTs towards GOR due to an increase in disorder due to unzipping. The 2D-band being an overtone of the D-band due to two-phonon scattering on a continuous graphene domain[50,51] could be observed in CNTs but is absent after unzipping due to incomplete exfoliation of the staged graphene sheets. Both oxidative unzipping of CNTs to produce GOR and the modified Hummers method result in organic functionalities such as hydroxyl, carboxylic acid, keto, and epoxy groups attached to the carbon sheets, which result in structural defects as shown in the schematics of Fig. 2b and c. Fourier transform infrared (FTIR) spectra (Fig. S3†) confirm the above organic linkages. The carboxylic (–COOH) and hydroxyl (–OH) groups give rise to the broad peak at 3000–3700 cm^{-1}, and the peak at 1600–1750 cm^{-1} is due to both ketonic C=O stretching and sp^2 C=C stretching frequencies. Due to the higher fraction of C=O in GOR the peak intensity also increases compared to CNT. The vibration modes of epoxide (C–O–C) in GO and GOR are also observed at 1084 and 1387 cm^{-1}.[52,53] The optical band gap of GOR calculated from the UV-vis spectra (Fig. S4†) is ~3.45 eV.

2.2 Photovoltaic performance of Cu_xS nanostructure CEs

The Cu_xS nanostructures deposited on FTO substrates (Fig. S5†) were applied as CEs in the QDSSCs assembled with the CdS sensitized photoanode. Fig. 3a shows the current–voltage (J–V) characteristics for seven different CEs and Table 1 summarizes the photovoltaic parameters of the resulting QDSSCs. The device shows better performance with slightly copper rich films ($Cu_{1.18}S$) than excess copper ($Cu_{1.7}S$) or sulfur ($Cu_{0.24}S$) containing films. Without the addition of carbon nanostructures, the CE prepared with $Cu_{1.18}S$ shows the highest efficiency of ~3.05% with a corresponding open circuit voltage (V_{oc}), short circuit current density (J_{sc}) and FF of ~0.544 V, ~10.68 mA cm^{-2} and ~0.53, respectively. Electrochemical impedance spectroscopy (EIS) measurements on symmetric cells of the CE material were performed to analyze the photovoltaic performance. The Nyquist plots are shown in Fig. 3b and R_s and R_{CT} extracted from the equivalent circuit (inset of Fig. 3b) are summarized in Table 1.[37] Being a p-type material the electrical conductivity of Cu_xS is a signature of the free holes created by Cu-vacancies and, accordingly, with decreasing x, the electrical conductivity should also increase.[54] According to the R_s and R_{CT} values, although this analogy holds true for Cu/S ratios from $Cu_{1.7}S$ to $Cu_{1.18}S$, an opposite trend is followed at higher Cu-deficiencies up to $Cu_{0.24}S$. In fact, moving away from x = 1.18, Cu-rich films show better charge transfer kinetics than S-rich films. The nanoplate thickness does not show a systematic trend with Cu:S stoichiometry, still the roughness of these nanoplates with lower sulphur content can play a role in increasing the catalytically active sites. At x < 1.18, the smoother nanoplates cannot possess enough catalytic sites, which likely overrides the factor of the generation of a larger number of free holes from higher Cu-vacancies. Therefore, with decreasing Cu/S ratio the range of variation of R_s is only from 2.49 to 1.62 Ω and again rises with a high excess of sulphur, hence R_s does not have a great impact on the QDSSC performance. The main contribution

Table 1 QDSSC parameters derived from *J–V*, impedance and Tafel plots

Sample name	V_{oc} (V)	J_{sc} (mA cm^{-2})	FF	η [a] (%)	R_s (Ω)	R_{CT} (Ω)	J_o (mA cm^{-2})	J_{lim} (mA cm^{-2})
$Cu_{1.7}S$	0.512	8.92	0.56	2.61 ± 0.08	2.49	18.01	0.49	5.52
$Cu_{1.42}S$	0.540	10.07	0.50	2.74 ± 0.04	2.23	22.53	0.47	5.37
$Cu_{1.23}S$	0.537	10.05	0.54	2.91 ± 0.05	1.93	11.5	0.57	7.58
$Cu_{1.18}S$	0.544	10.68	0.53	3.05 ± 0.06	1.68	10.15	0.67	8.31
$Cu_{1.03}S$	0.525	9.76	0.48	2.44 ± 0.10	1.65	15.93	0.39	3.71
$Cu_{0.94}S$	0.519	7.91	0.55	2.41 ± 0.09	1.62	26.33	0.32	2.75
$Cu_{0.24}S$	0.494	9.55	0.61	2.36 ± 0.11	2.83	27.48	0.23	1.44

[a] The efficiency data shown are the average values obtained from 3 devices.

towards PCE is from the interfacial charge transfer resistance (R_{CT}) associated with the CE. Since R_{CT} is the lowest for $Cu_{1.18}S$, the charge transfer from the polysulfide electrolyte to the CE is faster, reflecting its superior PCE.

2.3 Electrochemical analysis of Cu_xS nanostructures

The electrochemical activity of the Cu_xS nanostructures was investigated in terms of Tafel polarization and cyclic voltammetry (CV) studies. Fig. 3c shows the Tafel plots of symmetric cells for different Cu_xS films. The Tafel polarization measurement gives information on charge transfer kinetics. The exchange current density (J_o) estimated from the extrapolated intercepts of the anodic and cathodic branches of the Tafel polarization curves is related to R_{CT} according to the following equation:[28,37]

$$J_o = \frac{RT}{nFR_{CT}} \quad (1)$$

where R is the gas constant, T is the absolute temperature, n is the number of electrons involved in the polysulfide reduction and F is the Faraday constant. The variation of J_o derived from the Tafel plots (Table 1) is in good agreement with the EIS results, reconfirming the smaller R_{CT} for the $Cu_{1.18}S$ electrode. The catalytic properties can also be derived from the limiting current density (J_{lim}), which is mainly the diffusion velocity of the ionic carriers (polysulfide) between the two electrodes. J_{lim} is related to the diffusion coefficient (D) by the relation:[36,38]

$$J_{lim} = \frac{2nCFD}{l} \quad (2)$$

where l is the electrolyte thickness, n is the number of electrons involved in the reduction of disulfide at CE, F is the Faraday constant, and C is the polysulfide concentration. J_{lim} is directly proportional to the diffusion of charge carriers, and the relatively high J_{lim} for the $Cu_{1.18}S$ CE (Table 1) relates to its higher catalytic activity towards polysulfide reduction. The electrocatalytic activity of the Cu_xS CEs was also cross-checked by the cyclic voltammetry (CV) analysis in a three electrode setup (Fig. 3d). Since the positive and negative currents correspond to the oxidation of S^{2-} ions and the reduction of S_n^{2-} ions in the redox polysulfide electrolyte,[37] the relatively high reduction peak current densities of $Cu_{1.18}S$ electrodes reflect its agreement with the parameters obtained from Tafel plots. The next step will be to increase the FF of the QDSSCs with a composite CE of $Cu_{1.18}S$ and the carbon nanostructure.

2.4 Solar cell characteristics and EIS analysis of the composite CEs

For testing the most suitable carbon nanostructure, 10 wt% of either CNT, GO or GOR were mixed with $Cu_{1.18}S$ and the composite CEs termed as $Cu_{1.18}S$–CNT, $Cu_{1.18}S$–GO and $Cu_{1.18}S$–GOR, respectively. Although the XRD patterns of the composites exhibit the hexagonal covellite structure of $Cu_{1.18}S$, due to a low wt% of the carbon counterparts, a relatively weak (001) reflection is observed for CNT, GO and GOR (Fig. S6†). The CNT composite still exhibits the additional (002) hump. In contrast, the Raman spectra show the typical D- and G-bands of carbon without any observable vibration mode of $Cu_{1.18}S$ (Fig. S6†). The *J–V* characteristics of the FTO/TiO_2/CdS photoanode show significant improvement in FF and PCE with both $Cu_{1.18}S$–GO and $Cu_{1.18}S$–GOR (Fig. 4a and Table 2), although CNTs did not help to increase the PCE. In the case of $Cu_{1.18}S$–GOR CE, the maximum FF of 0.57 and increased device efficiency up to 3.38% are achieved. A possible reason for such an improvement in the device performance is the presence of highly catalytic crystalline edges of GOR (shown later in Fig. 5a), which effectively takes part in the polysulfide reduction process. Comparing this aspect with the morphology of CNT and GO (Fig. 2c and d), GOR has larger edge sites with attached functional groups (Fig. S3†) than CNT and GO, which helps faster reduction kinetics.[55,56] From a general perspective, the presence of edge sites in GOR is apparent since unzipping along the cylindrical morphology of the CNT will result in a higher number of dangling bonds at the unzipped edges which should be catalytically active. Also the quasi-1D structure of GOR helps in faster electron transfer through the 1D channel and therefore increases the device efficiency. The performance of the composite CEs was found to be far superior with respect to the conventional Pt and brass/Cu_2S CE (Table 2). The R_s values in Table 2 obtained from the Nyquist plots (Fig. 4b) of EIS measurements for the three composite CEs are slightly higher than those for Pt and brass/Cu_2S CEs (Fig. 4b, inset), due to the metallic nature of the latter. In fact, the large R_{CT} of Pt (1988 Ω) and brass/Cu_2S (1588 Ω) has a huge impact on the QDSSC performance. Interestingly, $Cu_{1.18}S$–GOR shows the lowest R_{CT} (1.26 Ω) as compared to $Cu_{1.18}S$–GO (1.63 Ω) and $Cu_{1.18}S$–CNT (3.17 Ω) which is also less than $Cu_{1.18}S$ (10.15 Ω) itself. Since R_{CT} is related to the charge transfer at the CE–electrolyte interface, lower R_{CT}

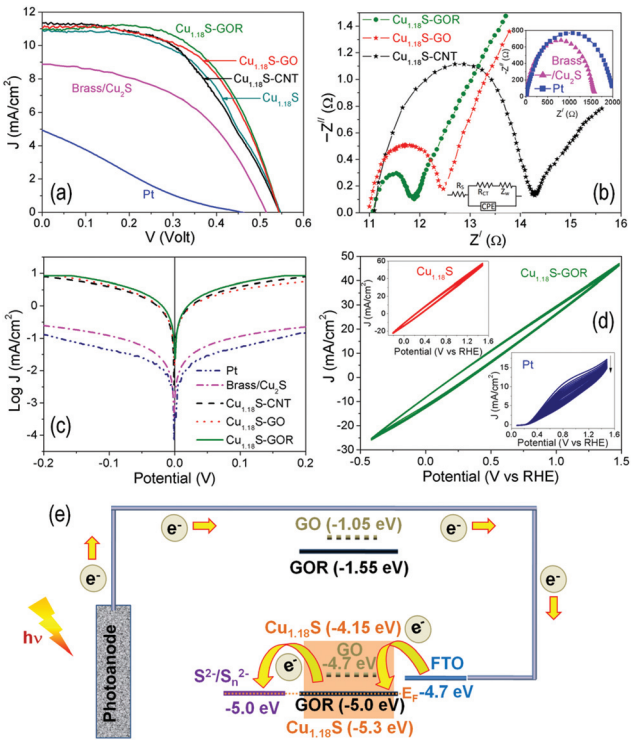

Fig. 4 (a) *J–V* characteristics, (b) Nyquist plot and (c) Tafel polarization characteristics of Pt, brass/Cu_2S and $Cu_{1.18}S$ composites with 10 wt% CNT, GOR and GO. (d) Stability tests: 50 cycles of CV plots for $Cu_{1.18}S$–GOR as the working electrode in a three electrode cell. The insets show the CV plots of the $Cu_{1.18}S$ working electrode for 50 cycles and Pt for 10 cycles, with an arrow showing the downward shift in current density over an increasing number of cycles. (e) Energy band diagram (not to scale) of $Cu_{1.18}S$–GOR CE showing electron transfer. The energy levels of GO are also indicated.

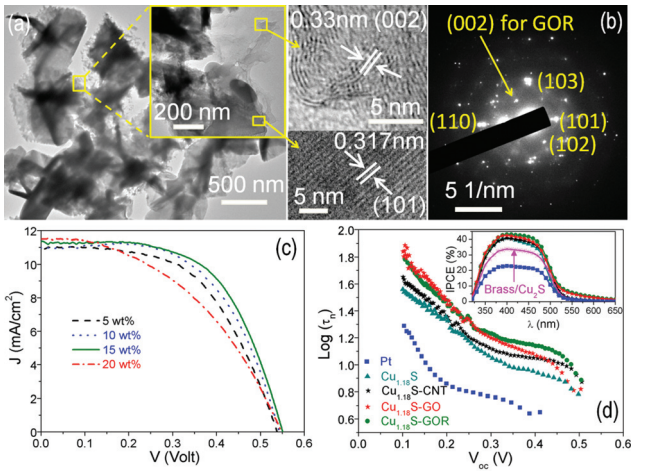

Fig. 5 (a) TEM micrograph of the 15 wt% GOR and $Cu_{1.18}S$ composite. The magnified regions show inter-planar spacing. (b) SAED patterns from the composite show the indexed crystallographic planes of $Cu_{1.18}S$. The (002) plane corresponds to GOR. (c) *J–V* characteristics for different GOR wt% in the $Cu_{1.18}S$–GOR composite CE. (d) Photogenerated charge carrier lifetime from V_{oc} decay for the composite CEs, $Cu_{1.18}S$ and Pt. The inset shows the IPCE spectra.

signifies higher charge transfer kinetics, which helps in improving the PCE with the $Cu_{1.18}S$–GOR CE.

2.5 Tafel plots and CV analysis of the composite CEs

Fig. 4c shows the Tafel plots of symmetric cells for all the CEs discussed above. The $Cu_{1.18}S$–GOR CE shows the highest J_o (Table 2), which according to eqn (1) relates to the lowest R_{CT} obtained from EIS measurements. Also J_{lim} is higher for the $Cu_{1.18}S$–GOR CE (Table 2), which implies larger diffusion of charge carriers following eqn (2). Since stability has been a major issue of CE for several years,[36] consecutive 50 CV cycles were tested in a conventional three electrode cell with the polysulfide electrolyte for both $Cu_{1.18}S$ and $Cu_{1.18}S$–GOR electrodes with excellent results (Fig. 4d). In contrast, a Pt working electrode with only 10 cycles shows a downward shift indicating poor stability owing to the poisoning effect of sulfur ions on Pt.[22] The superiority of the $Cu_{1.18}S$–GOR CE over Pt or $Cu_{1.18}S$–CNT, $Cu_{1.18}S$–GO composite CEs could be better understood from the parameters obtained from CV analyses (Table S7†). The electrochemical active surface area (ECSA) was calculated from the CV plots (Discussion and Fig. S7†) according to a standard protocol.[57,58] $Cu_{1.18}S$–GOR exhibits an ECSA of 575.2 $cm^2\ mg^{-1}$, higher than 538.0, 420.2 and 264.7 $cm^2\ mg^{-1}$ for $Cu_{1.18}S$–GO, $Cu_{1.18}S$–CNT and Pt, respectively. Higher ECSA of $Cu_{1.18}S$–GOR CE results in better interaction with the polysulfide electrolyte. Moreover, the relatively high negative current density (−25.35 mA cm^{-2}) of $Cu_{1.18}S$–GOR CE also confirms its superior catalytic activity towards the reduction process.

So far it has been obvious that the higher electrocatalytic activity of $Cu_{1.18}S$–GOR CE is the prime reason for its superior performance in increasing the PCE. In fact, the band diagram

Table 2 QDSSC parameters for five different CEs derived from *J–V*, impedance and Tafel plots. The composite CEs with $Cu_{1.18}S$ are with 10 wt% CNT, GOR and GO

Sample name	V_{oc} (V)	J_{sc} (mA cm^{-2})	FF	η [a] (%)	R_s (Ω)	R_{CT} (Ω)	J_o (mA cm^{-2})	J_{lim} (mA cm^{-2})
$Cu_{1.18}S$–CNT	0.543	11.35	0.50	3.1 ± 0.04	11.16	3.17	0.274	7.24
$Cu_{1.18}S$–GOR	0.543	10.92	0.57	3.38 ± 0.05	11.02	1.26	0.467	9.12
$Cu_{1.18}S$–GO	0.543	11.08	0.53	3.22 ± 0.02	10.95	1.63	0.350	8.12
Pt	0.458	5.34	0.21	0.5 ± 0.02	9.95	1988	0.005	0.24
Brass/Cu_2S	0.514	9.6	0.50	2.48 ± 0.10	10.58	1544	0.010	0.14

[a] The efficiency data shown are the average values obtained from 3 devices.

explanation (Fig. 4e) based on the available literature also justifies the experimental observations.[16,40] The standard reduction potential for polysulfide (S_n^{2-}/S^{2-}) is −5.0 eV from the vacuum level.[16] The valence band maximum for CuS is −5.3 eV and the highest occupied molecular orbital (HOMO) level of GOR as measured by Dai *et al.*[40] is −5.0 eV. Because of the p-type nature of Cu_xS the Fermi level (E_F) will be close to the valence band and will be in equilibrium with the reduction potential of the polysulfide under dark conditions. Since the HOMO level of GOR also matches with the reduction potential of polysulfide, it closely overlaps with the E_F of Cu_xS (Fig. 4e). GOR helps in increasing the number of available states close to its HOMO level facilitating the electron transfer, whereas Cu_xS actually participates in the reduction process. In QDSSCs, when the electron will move from the photoanode to CE to reduce the polysulfide, if the redox potential for polysulfide is closer to the HOMO level of GOR it will supply the electrons faster than $Cu_{1.18}S$ itself. This particular band alignment will therefore reduce the carrier loss and hence increase the PCE. The optical band gap of GO calculated from the UV-vis spectra is ~3.65 eV (Fig. S8†). Although the HOMO level of GO matches well with the Fermi level of the FTO contact (both ~−4.7 eV),[59,60] it is slightly higher above the redox potential of the polysulfide, which makes the transfer of electrons a little stringent compared to GOR.

2.6 Optimization of the composite CE and photovoltaic parameters

A TEM image of a representative composite with 15 wt% GOR and $Cu_{1.18}S$ is shown in Fig. 5a, where GOR wraps around the $Cu_{1.18}S$ plates shown by undulated nanoplate edges with lower contrast. GOR is observed to have graphitic edges and the composite as a whole is perfectly crystalline (Fig. 5a and b). The following step to improve the device performance is to alter the GOR wt% in the $Cu_{1.18}S$–GOR CEs. Fig. 5c shows the *J*–*V* curves for four different GOR percentages wherein PCE increases up to 15 wt% GOR and then decreases (Table 3). Since $Cu_{1.18}S$ is the reducing agent of oxidized polysulfide and GOR acts as the medium of charge transport between the $Cu_{1.18}S$ domains and then to FTO, excess GOR will block the active catalytic sites and decrease the electrochemical activity of $Cu_{1.18}S$. With 15 wt% GOR, the maximum PCE of 3.55% with a V_{oc} of ~0.551 V and a J_{sc} of ~11.33 mA cm^{-2} was achieved. The photogenerated charge carrier lifetime (τ_n) can be extracted from V_{oc} decay measurements using the equation:[14]

$$\tau_n = \frac{kT}{q}\left[\frac{dV_{oc}}{dt}\right]^{-1} \quad (3)$$

where *k* is the Boltzmann constant, *q* the elemental charge, and *T* the absolute temperature. Fig. 5d shows the plots of τ_n *versus* V_{oc}, and the actual decay curves of QDSSCs with CEs consisting of a composite of $Cu_{1.18}S$ with 15 wt% each of CNT, GO and GOR are shown in Fig. S9.† The faster decay corresponds to fast recombination kinetics and higher loss of charge carriers. From the decay curve it is evident that $Cu_{1.18}S$–GOR has the slowest decay owing to less recombination kinetics whereas Pt has the fastest decay. Considering the maximum power point condition (where $V_{oc} \sim 0.4$ V) in Fig. 5d, τ_n is also maximum for the $Cu_{1.18}S$–GOR CE. With 15 wt% GOR, the catalytically active $Cu_{1.18}S$–GOR CE experiences less R_{CT} in polysulfide reduction and hence it can reduce S_n^{2-} to S^{2-} ions faster leading to lower recombination losses and higher τ_n. The incident photon-to-current conversion efficiency (IPCE) spectra for different CEs exhibit a superior photoresponse over the range from 300 to 550 nm (Fig. 5d, inset). Although the IPCE spectra for $Cu_{1.18}S$ and its composites with 15 wt% CNT, GO and GOR do not show significant differences, they are far

Table 3 QDSSC parameters for $Cu_{1.18}S$–GOR CEs with different weight percentages of GOR

$Cu_{1.18}S$–GOR GOR (wt%)	V_{oc} (V)	J_{sc} (mA cm^{-2})	FF	η [a] (%)
5	0.538	10.94	0.55	3.22 ± 0.09
10	0.543	10.98	0.57	3.38 ± 0.05
15	0.551	11.33	0.58	3.55 ± 0.07
20	0.548	11.51	0.44	2.80 ± 0.12

[a] The efficiency data shown are the average values obtained from 3 devices.

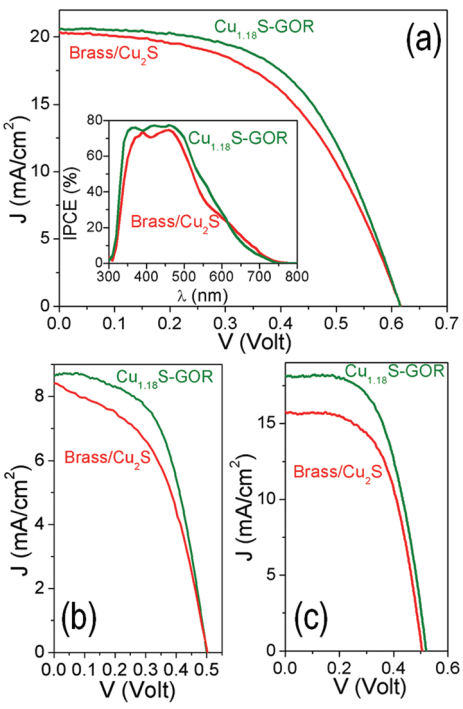

Fig. 6 *J*–*V* characteristics showing the improvement of PCE with $Cu_{1.18}S$–GOR CE for (a) CdTe/CdS/CdS core/shell/quasi-shell, (b) Mn-doped CdS, and (c) CdS/CdSe photoanodes. The inset in (a) shows the corresponding IPCE spectra.

Table 4 Photovoltaic parameters for different photoanodes and CEs providing a comparison of $Cu_{1.18}S$–GOR with the literature reported CEs. Here $Cu_{1.18}S$–GOR represents a composite with 15 wt% GOR

QDs	CEs	V_{oc} (V)	J_{sc} (mA cm^{-2})	FF	η (%)	Ref.
CdTe/CdS/CdS	Brass/Cu_2S	0.630	20.31	0.50	6.32	14
	$Cu_{1.18}S$–GOR	0.626	20.55	0.53	6.81	This work
Mn:CdS	Brass/Cu_2S	0.501	8.39	0.49	2.08	60
	$Cu_{1.18}S$–GOR	0.501	8.64	0.56	2.42	This work
CdS/CdSe	CuS	0.42	9.38	0.37	1.47	30
	Cu_2S	0.54	11.70	0.48	3.04	25
	Carbon–Cu_2S	0.49	10.70	0.58	3.08	62
	Cu_2S	0.60	11.69	0.44	3.18	63
	$Cu_{1.8S}$/CuS	0.54	14.50	0.41	3.22	64
	RGO–Cu_2S	0.52	18.40	0.46	4.40	18
	Brass/Cu_2S	0.504	15.66	0.56	4.50	This work
	$Cu_{1.18}S$–GOR	0.520	18.04	0.58	5.42	This work

superior with respect to Pt or brass/Cu_2S CEs. Since IPCE is directly related to the photocurrent and there are minimal differences in J_{sc} with different composite CEs, IPCE also follows suit.

2.7 Improvement of previously reported PCEs

When $Cu_{1.18}S$–GOR is used as the CE on previously reported CdTe/CdS/CdS core/shell/quasi-shell QDSSC,[14] the PCE improves to 6.81% from earlier reported 6.32% using the brass/Cu_2S CE (Fig. 6a) due to a proportionate increase in FF from 0.50 to 0.53 (Table 4). Fig. 6a (inset) shows the corresponding IPCE characteristics with brass/Cu_2S and $Cu_{1.18}S$–GOR CEs, where the photo-response is observed from 300 to 750 nm with a small enhancement in IPCE. In addition, the PCE of 1.44 at% Mn doped CdS QDSSC[61] is also improved from 2.08 to 2.42% with an increase in FF from 0.49 to 0.56 (Fig. 6b and Table 4). The performance of $Cu_{1.18}S$–GOR CE is also evaluated with respect to other reported CEs with a common SILAR deposited CdS/CdSe co-sensitized photoanode. The $Cu_{1.18}S$–GOR CE achieves a record PCE of 5.42% with a V_{oc} of ~0.52 V and a J_{sc} of ~18.04 mA cm^{-2} (Fig. 6c), higher than the PCEs reported with other CEs (Table 4).[18,25,30,62–64]

3. Conclusions

In conclusion, a highly efficient electrocatalytic CE for QDSSCs was designed through a composite of microwave synthesized $Cu_{1.18}S$ nanostructures and 15 wt% GOR, prepared by unzipping MWCNTs. Seven different compositions of Cu_xS were tested by photovoltaic and electrocatalytic performance to determine the best performing stoichiometry of x = 1.18. The composite of GOR with $Cu_{1.18}S$ was found to be superior with respect to those with CNT and GO, due to higher functionalization, graphitic edge sites and quasi-1D structure in GOR. The reasons pertaining to better photovoltaic performance have been elucidated by EIS analysis and the electrocatalytic performance by Tafel polarization and CV studies. The high electrocatalytic activity of GOR could be retained after several cycles, maintaining a low R_{CT} for efficient electron transfer from the CE to the polysulfide electrolyte. A record PCE ~3.55% for SILAR deposited CdS sensitized QDSSC was achieved, apart from a significant increase in PCE of reported QDSSCs. Moreover, the comparison of different CEs in the case of CdS/CdSe co-sensitized QDSSC has demonstrated the superiority of $Cu_{1.18}S$–GOR CE. However, there is enough room to further optimize the CEs for improved QDSSC performance and research is underway in this direction.

4. Experimental details

4.1 Materials

$Cu(NO_3)_2{\cdot}3H_2O$ (≥99%), sulfur powder (99%), ethylene glycol (≥99%), cadmium acetate dihydrate (≥99%), potassium chloride (99%), sodium sulphide flakes (≥50%), zinc acetate dihydrate (≥99%), sulfuric acid (98%), ethanol (absolute), and titanium tetrachloride (99%) were purchased from Merck, India. MWCNT (≥95%) was purchased from SRL Pvt. Ltd, Mumbai, India. 1-Methyl-2-pyrrolidone (NMP, 99%), $Zn(NO_3)_2{\cdot}6H_2O$ (98%), and polyvinylidene fluoride (PVDF) powder were purchased from Sigma Aldrich. F:SnO_2 (FTO)-coated glass (TCO 22-7), TiO_2 paste (Ti-nanoxide T/SP, average size ~20 nm), and scattering TiO_2 paste (Ti-nanoxide R/SP, average size >100 nm) were purchased from Solaronix. Graphite powder (99.99%) and a brass foil (0.25 mm thick) were purchased from Alfa Aesar. All reagents were used as received.

4.2 Methods

4.2.1. Synthesis of Cu_xS nanostructures. A flux of 5 mmol $Cu(NO_3)_2{\cdot}6H_2O$ and 5 mmol sulfur powder in 100 mL ethylene glycol was irradiated in a microwave chamber for 12 min at 600 W and 125 °C with constant stirring at 2000 rpm. For different Cu/S ratios the solution turned from deep green to greyish and the grey product was centrifuged at 6500 rpm for 15 min, washed with ethanol and dried at 80 °C for 1.5 h to obtain the Cu_xS nanostructures.

4.2.2. Synthesis of GOR and GO. GOR was synthesized modifying the procedure of Dai *et al.*[40] 50 mg MWCNTs was bath sonicated in 50 mL 98% H_2SO_4 for 30 min and stirred overnight at room temperature. 250 mg 500 wt% $KMnO_4$ was added to this dispersion slowly over 2 h under constant stirring at room temperature followed by additional stirring at 70 °C for 2 h during which 100 mg $KMnO_4$ was added slowly and the colour changed from grey to dark brown indicating completion of the reaction. The reaction mixture was allowed to cool to room temperature and poured into a mixture of 150 ml ice and 2.5 mL H_2O_2 under stirring. Finally, the resultant dispersion was diluted by adding 2 L of cold distilled ionized (DI) water and vacuum filtered through a PTFE membrane (0.45 μm pore size). The product was removed and stirred in 100 mL ethanol for 30 min. The final product was washed twice with ethanol to obtain the dried GOR as a dark precipitate.

GO was prepared by a modified Hummers method.[65] The mixture of 1 g graphite powder, 0.5 g $NaNO_3$ and 25 mL conc. H_2SO_4 was cooled to 0 °C in an ice bath and stirred for 2 h. 3 g $KMnO_4$ was added slowly with continuous stirring for another 1 h, followed by 30 mL DI water at room temperature. The temperature of the mixture was then increased to 90 °C in an oil bath and 100 mL DI water was added under continuous stirring for 1 h until the colour of the mixture turned to mud brown. The mixture was further treated with 10 mL 30% H_2O_2, diluted with 2.5 L excess DI water, filtered and, after drying overnight under vacuum conditions, GO was collected.

4.2.3. Preparation of QD-sensitized photoanodes. FTO coated glass was washed in a soap solution, DI water, and ethanol under sonication for 20 min each. A compact TiO_2 layer was deposited on the FTO glass by dip coating in 40 mM $TiCl_4$ solution at 80 °C for 40 min and washed with DI water and ethanol. A 8 μm thick mesoporous TiO_2 active layer was then doctor-bladed onto the compact TiO_2 layer coated FTO and dried at 80 °C for 30 min, followed by annealing at 500 °C for 1 h in a box furnace. A 4 μm thick scattering TiO_2 layer was similarly doctor bladed on top of the active layer and annealed at 500 °C for 1 h.

CdS photoanode. CdS QDs were deposited through the SILAR process. In brief, the TiO_2 films were dipped alternately in a 0.1 M methanol solution of $Cd(OAc)_2{\cdot}2H_2O$ and a 0.1 M methanol : water (1 : 1) solution of $Na_2S{\cdot}9H_2O$ for 1 min. The films were washed with DI water and dried in air between each step to complete one SILAR cycle. The total number of CdS SILAR cycles was 8, followed by two SILAR cycles of a ZnS passivation layer deposited from 0.1 M aqueous solutions of $Zn(NO_3)_2{\cdot}6H_2O$ and $Na_2S{\cdot}9H_2O$, respectively. Finally, the films were washed with excess amounts of DI water and allowed to dry in air at room temperature.

The CdTe/CdS/CdS core/shell/quasi-shell sensitizer. CdTe/CdS core/shell QDs were prepared according to our previous report.[14] In brief, the mercaptopropionic acid capped core/shell QDs were deposited on TiO_2 coated FTO glass by dipping into this sensitizing solution with pH ~ 13 for 12 h and washed sequentially with DI water and ethanol. After loading the pre-synthesized core/shell QDs, the CdS quasi-shell was deposited through 4 cycles of SILAR and 2 cycles of ZnS and finally washed and dried at room temperature.

The Mn-doped CdS QD sensitizer. Mn-doped CdS QDs were also prepared according to our previous report.[61] In brief, the degassed solution of 1 mmol $CdCl_2{\cdot}H_2O$, $MnCl_2{\cdot}4H_2O$ (Mn:Cd at% 1.44) and 5 mL of oleylamine was heated and aged at 100 °C for 30 min followed by the injection of sulfur–oleylamine solution at 170 °C. The colloidal solution was aged at 170 °C for 70 min followed by cooling the flask to room temperature, precipitation of the product with isopropanol, centrifugation, and washing with ethanol to obtain the QDs finally suspended in chloroform. The Mn-doped CdS QDs were deposited on the FTO/TiO_2 photoanode by electrophoretic deposition.[61]

CdS/CdSe photoanode. Firstly, the TiO_2 film on FTO was alternately dipped into a 0.1 $Cd(OAc)_2$ and 0.1 M Na_2S solution five times for 1 min in each dipping cycle. Secondly, the TiO_2/CdS film was dipped into a bath of 0.1 M $Cd(OAc)_2$ and Na_2SeSO_3 solution for 3 h. The aqueous solution of Na_2SeSO_3 was prepared by refluxing 0.1 M Se and 0.2 M Na_2SO_3 in an aqueous solution at 100 °C for 3 h. Finally, the TiO_2/CdS/CdSe electrodes were passivated with ZnS by alternate dipping into 0.1 M $Zn(NO_3)_2$ and 0.1 M Na_2S solutions two times for 2 min for each dipping cycle.

4.2.4. Preparation of CE. A paste of Cu_xS was prepared by stirring overnight a mixture of 100 mg of Cu_xS nanostructures, 10 mg PVDF and 300 μL NMP. The paste was doctor bladed on pre-cleaned FTO with a layer thickness of ~2 μm, dried and annealed at 80 °C for 1.5 h. The composites of Cu_xS with GOR, GO and MWCNT were prepared by making a similar paste of Cu_xS and GOR/GO/MWCNT in different proportions. The Pt electrode was prepared by doctor blading platisol (T/SP, Solaronix) on cleaned FTO followed by annealing at 500 °C for 1 h. The Cu_2S on brass foil counter electrodes (named as brass foil) were prepared by immersing a brass foil in HCl solution at 70 °C for 10 min followed by vulcanization using the polysulfide electrolyte solution. The polysulfide electrolyte solution consists of 2 M Na_2S, 2 M S, and 0.2 M KCl in a methanol–water (1 : 1, v/v) solution.

4.2.5. Device fabrication. The solar cell devices were prepared by assembling the QD-sensitized photoanode and counter electrode using a parafilm spacer (50 μm) in a sandwich configuration. A 80 μL droplet of the polysulfide electrolyte was employed between the two electrodes before assembling them. The active area of the working electrodes was 0.23 cm^2.

4.2.6. Characterization. The FESEM images were recorded using a Carl Zeiss SUPRA 55VP FESEM. EDAX spectra were recorded with an Oxford Instruments X-Max with the INCA software coupled to the FESEM. The XRD measurements were carried out with a Rigaku (Mini Flex II, Japan) powder X-ray diffractometer having Cu Kα = 1.54059 Å radiation. TEM images were obtained with a UHR-FEG TEM system (JEOL, Model JEM 2100 F) using a 200 kV electron source. A LABRAM HR800 Raman spectrometer was employed using the 633 nm

line of a He–Ne ion laser as the excitation source to analyze the nanostructures. FTIR studies were performed with a Perkin Elmer spectrum RX1 with KBr pellets. UV-vis absorbance spectra were recorded using a Jasco Model V-670 spectrophotometer equipped with an integrating sphere. Photovoltaic performances (*J–V* curves) of QDSSCs were measured using an electrochemical workstation (CH Instruments, Model CHI604D), and the illumination source was a 150 W AM 1.5G solar simulator (Newport, Model no. 65007). The intensity of the simulated solar light was calibrated to 100 mW cm^{-2} using a standard silicon solar cell (NREL). EIS measurements were performed by making a symmetric dummy cell on a workstation (CH Instruments, Model CHI604D) in the dark at zero bias, with a frequency ranging from 1 MHz to 0.1 Hz. Tafel polarization characteristics were also measured on the dummy cells with a scan rate of 50 mV s^{-1}. Open circuit voltage decay measurements were performed by illuminating the cell until a steady photovoltage was registered, after which the illumination was instantaneously switched off while monitoring the change in V_{oc} with time. IPCE spectra were recorded using a Newport Apex monochromator illuminator. The CV studies were performed with a conventional three electrode cell in a CHI604D electrochemical workstation. The three electrode cell was assembled by using a Pt wire as the counter electrode, a saturated Ag/AgCl as the reference electrode and a Cu_xS or Cu_xS–GOR on FTO as the working electrode. The scanning rate was maintained constant at 50 mV s^{-1}.

Acknowledgements

D. G. acknowledges the Department of Science and Technology (DST) India-Israel S&T Cooperation for his fellowship. The Department of Science and Technology (DST) Indo-Israeli S&T Programme of Cooperation is duly acknowledged for the financial support, under Sanction No. DST/INT/ISR/P-11/2014. GH thanks University Grants Commission (UGC), New Delhi for her fellowship. A. S. thanks the academic and research funding of IISER Kolkata for his fellowship.

References

1 K. Zhao, Z. Pan, I. Mora-Seró, E. Cánovas, H. Wang, Y. Song, X. Gong, J. Wang, M. Bonn, J. Bisquert and X. Zhong, *J. Am. Chem. Soc.*, 2015, **137**, 5602–5609.
2 A. Loiudice, A. Rizzo, G. Grancini, M. Biasiucci, M. R. Belviso, M. Corricelli, M. L. Curri, M. Striccoli, A. Agostiano, P. D. Cozzoli, A. Petrozza, G. Lanzanidh and G. Gigli, *Energy Environ. Sci.*, 2013, **6**, 1565–1572.
3 J. A. Christians, R. C. M. Fung and P. V. Kamat, *J. Am. Chem. Soc.*, 2014, **136**, 758–764.
4 Z. X. Pan, I. Mora-Sero, Q. Shen, H. Zhang, Y. Li, K. Zhao, J. Wang, X. H. Zhong and J. Bisquert, *J. Am. Chem. Soc.*, 2014, **136**, 9203–9210.
5 P. V. Kamat, K. Tvrdy, D. R. Baker and J. G. Radich, *Chem. Rev.*, 2010, **110**, 6664–6688.
6 I. Mora-Seró, S. Giménez, T. Moehl, F. Fabregat-Santiago, T. Lana-Villareal, R. Gómez and J. Bisquert, *Nanotechnology*, 2008, **19**, 424007.
7 J. Xu, Z. H. Chen, J. A. Zapien, C. S. Lee and W. J. Zhang, *Adv. Mater.*, 2014, **26**, 5337–5367.
8 Z. Pan, K. Zhao, J. Wang, H. Zhang, Y. Feng and X. Zhong, *ACS Nano*, 2013, **7**, 5215–5222.
9 C. Giansante, L. Carbone, C. Giannini, D. Altamura, Z. Ameer, G. Maruccio, A. Loiudice, M. R. Belviso, P. D. Cozzoli, A. Rizzo and G. Gigli, *J. Phys. Chem. C*, 2013, **117**, 13305–13317.
10 Z. Ren, J. Wang, Z. Pan, K. Zhao, H. Zhang, Y. Li, Y. Zhao, I. Mora-Sero, J. Bisquert and X. Zhong, *Chem. Mater.*, 2015, **27**, 8398–8405.
11 G.-H. Kim, F. P. G. de Arquer, Y. J. Yoon, X. Lan, M. Liu, O. Voznyy, Z. Yang, F. Fan, H. Ip. Alexander, P. Kanjanaboos, S. Hoogland, J. Y. Kim and E. H. Sargent, *Nano Lett.*, 2015, **15**, 7691–7696.
12 P. K. Santra and P. V. Kamat, *J. Am. Chem. Soc.*, 2013, **135**, 877–885.
13 J. Wang, I. Mora-Seró, Z. X. Pan, K. Zhao, H. Zhang, Y. Y. Feng, G. Yang, X. H. Zhong and J. Bisquert, *J. Am. Chem. Soc.*, 2013, **135**, 15913–15922.
14 A. Sahasrabudhe and S. Bhattacharyya, *Chem. Mater.*, 2015, **27**, 4848–4859.
15 A. Loiudice, G. Grancini, A. Taurino, M. Corricelli, M. R. Belviso, M. Striccoli, A. Agostiano, M. L. Curri, A. Petrozza, P. D. Cozzoli, A. Rizzo and G. Gigli, *ACS Appl. Mater. Interfaces*, 2014, **6**, 5026–5033.
16 V. Chakrapani, D. Baker and P. V. Kamat, *J. Am. Chem. Soc.*, 2011, **133**, 9607–9615.
17 J. Xu, X. Yang, Q. D. Yang, W. J. Zhang and C. S. Lee, *ACS Appl. Mater. Interfaces*, 2014, **6**, 16352–16359.
18 J. G. Radich, R. Dwyer and P. V. Kamat, *J. Phys. Chem. Lett.*, 2011, **2**, 2453–2460.
19 V. González-Pedro, X. Xu, I. Mora-Seró and J. Bisquert, *ACS Nano*, 2010, **4**, 5783–5790.
20 F. Liu, J. Zhu, Y. Li, J. Wei, M. Lv, Y. Xu, L. Zhou, L. Hu and S. Dai, *J. Power Sources*, 2015, **292**, 7–14.
21 M. Seol, D. H. Youn, J. Y. Kim, J.-W. Jang, M. Choi, J. S. Lee and K. Yong, *Adv. Energy Mater.*, 2014, **4**, 1300775.
22 Z. Yang, C.-Y. Chen, C.-W. Liu, C.-L. Li and H.-T. Chang, *Adv. Energy Mater.*, 2011, **1**, 259–264.
23 M. D. Ye, C. Chen, N. Zhang, X. Wen, W. Guo and C. J. Lin, *Adv. Energy Mater.*, 2014, **4**, 1301564.
24 J. Xu, X. Yang, T. L. Wong and C. S. Lee, *Nanoscale*, 2012, **4**, 6537–6542.
25 Y. Jiang, X. Zhang, Q. Q. Ge, B. B. Yu, Y. G. Zou, W. J. Jiang, W. G. Song, L. J. Wan and J. S. Hu, *Nano Lett.*, 2014, **14**, 365–372.
26 G. S. Selopal, I. Concina, R. Milan, M. M. Natile, G. Sberveglieri and A. Vomiero, *Nano Energy*, 2014, **6**, 200–210.
27 C. Shen, L. Sun, Z. Y. Koh and Q. Wang, *J. Mater. Chem. A*, 2014, **2**, 2807–2813.

28 M. L. Que, W. X. Guo, X. J. Zhang, X. Y. Li, Q. L. Hua, L. Dong and C. F. Pan, *J. Mater. Chem. A*, 2014, **2**, 13661–13666.
29 M. S. Faber, K. Park, M. Cabán-Acevedo, P. K. Santra and S. Jin, *J. Phys. Chem. Lett.*, 2013, **4**, 1843–1849.
30 H. N. Chen, L. Q. Zhu, H. C. Liu and W. P. Li, *J. Phys. Chem. C*, 2013, **117**, 3739–3746.
31 C. Y. Lin, C. Y. Teng, T. L. Li, Y. L. Lee and H. S. Teng, *J. Mater. Chem. A*, 2013, **1**, 1155–1162.
32 Z. Tachan, M. Shalom, I. Hod, S. Rühle, S. Tirosh and A. Zaban, *J. Phys. Chem. C*, 2011, **115**, 6162–6166.
33 H. J. Yu, H. L. Bao, K. Zhao, Z. L. Du, H. Zhang and X. H. Zhong, *J. Phys. Chem. C*, 2014, **118**, 16602–16610.
34 M.-S. Fan, J.-H. Chen, C.-T. Li, K.-W. Cheng and K.-C. Ho, *J. Mater. Chem. A*, 2015, **3**, 562–569.
35 H. Zhang, H. Bao and X. Zhong, *J. Mater. Chem. A*, 2015, **3**, 6557–6564.
36 F. Liu, J. Zhu, L. Hu, B. Zhang, J. Yao, Md. K. Nazeeruddin, M. Gratzel and S. Dai, *J. Mater. Chem. A*, 2015, **3**, 6315–6323.
37 M. Ye, X. Wen, N. Zhang, W. Guo, X. Liua and C. Lin, *J. Mater. Chem. A*, 2015, **3**, 9595–9600.
38 V.-D. Dao, P. Kim, S. Baek, L. L. Larina, K. Yong, R. Ryoo, S. H. Ko and H.-S. Choi, *Carbon*, 2016, **96**, 139–144.
39 M. J. Allen, V. C. Tung and R. B. Kaner, *Chem. Rev.*, 2010, **110**, 132–145.
40 J. Liu, G.-H. Kim, Y. Xue, J. Y. Kim, J.-B. Baek, M. Durstock and L. Dai, *Adv. Mater.*, 2014, **26**, 786–790.
41 D. V. Kosynkin, A. L. Higginbotham, A. Sinitskii, J. R. Lomeda, A. Dimiev, B. K. Price and J. M. Tour, *Nature*, 2009, **458**, 872–877.
42 A. Giuri, S. Rella, M. Corricelli, S. Colella, A. Listorti, G. Gigli, A. Rizzo, P. D. Cozzoli, R. M. Acocella, G. Guerra and E. C. Corcione, *Sci. Adv. Mater.*, 2015, **7**, 2445–2451.
43 Md. A. Hossain, J. R. Jennings, C. Shen, J. H. Pan, Z. Y. Koh, N. Mathews and Q. Wang, *J. Mater. Chem.*, 2012, **22**, 16235–16242.
44 L. Mu, C. Liu, J. Jia, X. Zhou and Y. Lin, *J. Mater. Chem. A*, 2013, **1**, 8353–8357.
45 K. Zhao, H. Yu, H. Zhang and X. Zhong, *J. Phys. Chem. C*, 2014, **118**, 5683–5690.
46 L. Li, P. Zhu, S. Peng, M. Srinivasan, Q. Yan, A. S. Nair, B. Liu and S. Samakrishna, *J. Phys. Chem. C*, 2014, **118**, 16526–16535.
47 J. Zhang, H. Feng, J. Yang, Q. Qin, H. Fan, C. Wei and W. Zheng, *ACS Appl. Mater. Interfaces*, 2015, **7**, 21735–21744.
48 Y. Shengyuan, A. S. Nair, Z. Peining and S. Ramakrishna, *Mater. Lett.*, 2012, **76**, 43–46.
49 Y. Xie, L. Carbone, C. Nobile, V. Grillo, S. D'Agostino, F. D. Sala, C. Giannini, D. Altamura, C. Oelsner, C. Kryschi and P. D. Cozzoli, *ACS Nano*, 2013, **7**, 7352–7369.
50 A. Z. Yazdi, K. Chizari, A. S. Jalilov, J. Tour and U. Sundararaj, *ACS Nano*, 2015, **9**, 5833–5845.
51 K.-H. Wu, D.-W. Wang and I. R. Gentle, *Carbon*, 2015, **81**, 295–304.
52 L. Jiang, L. Sheng, C. Long, T. Wei and Z. Fan, *Adv. Energy Mater.*, 2015, **5**, 1500771.
53 Sudesh, N. Kumar, S. Das, C. Bernhard and G. D. Varma, *Supercond. Sci. Technol.*, 2013, **26**, 095008.
54 C. S. Kim, S. H. Choi and J. H. Bang, *ACS Appl. Mater. Interfaces*, 2014, **6**, 22078–22087.
55 S. Fujii, M. Ziatdinov, M. Ohtsuka, K. Kusakabe, M. Kiguchia and T. Enoki, *Faraday Discuss.*, 2014, **173**, 173–199.
56 J. Benson, Q. Xu, P. Wang, Y. Shen, L. Sun, T. Wang, M. Li and P. Papakonstantinou, *ACS Appl. Mater. Interfaces*, 2014, **6**, 19726–19736.
57 H.-Y. Du, C.-H. Wang, C.-S. Yang, H.-C. Hsu, S.-T. Chang, H.-C. Huang, S.-W. Lai, J.-C. Chen, T. L. Yu, L.-C. Chenc and K.-H. Chen, *J. Mater. Chem. A*, 2014, **2**, 7015–7019.
58 A. L. Ong, K. K. Inglis, D. K. Whelligan, S. Murphy and J. R. Varcoe, *Phys. Chem. Chem. Phys.*, 2015, **17**, 12135–12145.
59 J. Liu, M. Durstock and L. Dai, *Energy Environ. Sci.*, 2014, **7**, 1297–1306.
60 I. Mora-Sero, L. Bertoluzzi, V. Gonzalez-Pedro, S. Gimenez, F. Fabregat-Santiago, K. W. Kemp, E. H. Sargent and J. Bisquert, *Nat. Commun.*, 2013, **4**, 2272.
61 G. Halder and S. Bhattacharyya, *J. Phys. Chem. C*, 2015, **119**, 13404–13412.
62 M. H. Deng, Q. X. Zhang, S. Q. Huang, D. M. Li, Y. H. Luo, Q. Shen, T. Toyoda and Q. B. Meng, *Nanoscale Res. Lett.*, 2010, **5**, 986–990.
63 H. Salaramoli, E. Maleki, Z. Shariatinia and M. Ranjbar, *J. Photochem. Photobiol., A*, 2013, **271**, 56–64.
64 L. Quan, W. Li, L. Zhu, X. Chang and H. Liu, *RSC Adv.*, 2014, **4**, 32214–32220.
65 N. A. Kumar, S. Gambarelli, F. Duclairoir, G. Bidan and L. Dubois, *J. Mater. Chem. A*, 2013, **1**, 2789–2794.